

Phase field modeling of fracture in nonlinearly elastic solids via energy decomposition

Shan Tang^{a,b,c}, Gang Zhang^c, Tian Fu Guo^d, Xu Guo^{a,b,*}, Wing Kam Liu^{e,f,**}

^a State Key Laboratory of Structural Analysis for Industrial Equipment, Department of Engineering Mechanics, Dalian University of Technology, Dalian, 116023, PR China

^b International Research Center for Computational Mechanics, Dalian University of Technology, PR China

^c College of Aerospace Engineering, Chongqing University, Chongqing, 400017, China

^d Institute of High Performance Computing, A*STAR, Singapore, 138632, Singapore

^e Honorary professor, Dalian University of Technology, China

^f Department of Mechanical Engineering, Northwestern University, Evanston, IL, USA

Received 22 August 2018; received in revised form 24 December 2018; accepted 28 December 2018

Available online 6 January 2019

Abstract

Phase-field models for fracture problems have attracted considerable attention in recent years, which are capable of tracking the discontinuities numerically, and also produce complex crack patterns in many applications. In this paper, a phase-field model for a general nonlinearly elastic material is proposed using a novel additive decomposition of strain energy. This decomposition has two parts: one is principal stretch related and the other solely composed of volumetric deformation, which accounts for different behaviors of fracture in tension and compression. We construct the Lagrangian by integrating the split energies and the separation energy from phase-field approximation for discrete cracks. A coupled system of equations is also derived that governs the deformation of the body and the evolution of phase field. The capability and performance of the proposed model are demonstrated in several representative examples. Our results show that the predicted fracture surfaces are in good agreement with experimental observations. Compared with the previous models in which the energy is simply split into the isochoric and volumetric parts, the present model is numerically more robust and effective in simulating sharp cracks. The present model can also aid researchers to control the degree of tension–compression asymmetry in the nonlinear regime of deformation, which can be naturally extended to simulate the fracture of the rubber-like materials with tension–compression asymmetry.

© 2018 Elsevier B.V. All rights reserved.

Keywords: Energy decomposition; Hyperelastic materials; Fracture; Phase field

1. Introduction

The prediction of crack initiation, propagation, and fracture path of the rubber-like polymeric materials is important for many engineering applications. These rubber-like polymeric materials are widely found in synthesized engineering materials such as rubber, elastomer, and hydrogel [1–4], as well as in natural materials such as tissue, muscle or

* Corresponding author.

** Correspondence to: Department of Engineering Mechanics, Dalian University of Technology, Dalian, China.

E-mail addresses: guoxu@dlut.edu.cn (X. Guo), w-liu@northwestern.edu (W.K. Liu).

elastin [5–7]. These materials usually exhibit well-known complicated behaviors such as large and nonlinear elasticity, pressure-sensitive plasticity, and viscoelasticity. [8–13]. Recently, it is also found that some of these natural or synthesized polymeric materials demonstrate tension–compression asymmetry, whereby the elastic modulus under tension is different from that under compression [14,15]. In the engineering applications with these rubber-like polymeric materials, the structural integrity should be kept and the macroscopic crack should be prevented. Fracture mechanics for these rubber-like polymeric materials in the applications should be further developed.

The phase-field approach to modeling fracture has garnered considerable attention in recent years. This approach, also known as the variational approach to fracture, is able to simulate complex crack patterns such as crack intersection without having to model the discontinuity directly. This approach was first proposed by Francfort and Marigo [16], who approached the fracture problem by minimizing a potential energy based on the Griffith's theory of brittle fracture inspired by the works of Mumford and Shah [17] and Ambrosio and Tortorelli [18]. An alternative framework is formulated by Miehe et al. [19,20] based on continuum mechanics and thermodynamic arguments. Miehe et al. [19] also added an important mechanism to distinguish tensile and compressive effects on crack growth. This approach also has been extended to model dynamic fracture [21–25] and the obtained results show a good agreement with several benchmark problems. These mentioned works are confined to the small-deformation setting [26–28]. Extension of the phase-field method to consider the plasticity has been reported in [29,30] and [31], which found that the accumulation of plastic deformation can reduce the elastic strength with the plastic response remaining unaffected. A phase-field model for ductile fracture in the kinematically linear regime is extended to the three-dimensional finite strain setting by Ambati et al. [32]. The model is further improved by Borden et al. [33], which incorporates the micro-force derivation of the governing equation in terms of an energy potential at the finite deformation regime, the degrading yielding surface, and a mechanism to include a measure of stress triaxiality as a driving force for crack initiation and propagation.

In this work, we focus on modeling the fracture by means of phase field method at finite deformation elasticity, which serves as an initial step to model the complicated elastic–plastic behavior of these rubber-like polymeric materials that we discuss in the present work. Although Miehe and Schänzel [34] and recent work of Chen et al. [35] have modeled the fracture of hyperelastic solids at the finite deformation regime with the phase field approach, an artificial viscous regularization of the rate-independent formulation is introduced to stabilize the numerical simulation for which the tensile–compressive effects on the crack growth are not distinguished. To model the elastic part of the deformation in their phase-field frameworks for elastic–plastic materials, Borden et al. [33] and Arriaga and Waisman [36] decomposed the elastic deformation energy into volumetric and deviatoric parts to distinguish the tensile and compressive contributions to fracture, following [37] at the small deformation regime. However, based on [19] and [24], the spectral decomposition of the logarithmic strain tensor into tension or compression parts appears more appropriate [38]. However, it is pointed out by Borden et al. [33] that this approach may result in a loss of numerical accuracy and lead to convergence problems.

This paper presents a novel way to decompose the strain energy for phase field modeling of fracture in nonlinearly elastic solids. Unlike [19] and [24], we decompose the energy into two parts: one is principal stretch related and the other solely composed of a nonlinear term of volumetric deformation. This decomposition permits to identify the different roles taken by tension and compression in modeling the real fracture directly; namely it permits to describe the physical picture of fracture more realistically. On the other hand, we also revisit the phase field models which were originally developed for small-strain elastic materials [19,24] and later extended for finite strain [33,36]. In these models, the deformation energy is simply decomposed into the isochoric and volumetric parts. The Lagrangian for the discrete fracture problem in terms of displacement and the phase-field approximation of the crack is formulated in Section 2. The variation on the Lagrangian leads to the strong form equations of motion with the phase field. These equations are solved by C^0 -continuous finite elements. We study the behavior of the proposed model and the model adopted by Borden et al. [33] and Arriaga and Waisman [36] through performing a number of numerical experiments on crack propagation in Section 3. The morphology of fracture surface predicted by the current model agrees with experimental results available. Compared with the models adopted in [33] and [36], the present model enables robust numerical simulations. The paper will conclude with a short summary.

2. Material model and phase field formulation

In this section, a Bourdin-type phase field theory is formulated based on Griffith's theory within the framework of finite deformation [24,39]. Let us consider an arbitrary body B enclosed by the surface ∂B . During deformation, the

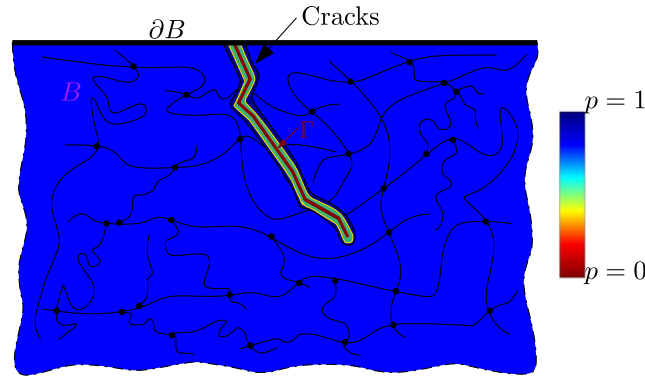


Fig. 1. Schematic representation of a solid body B with rubber-like polymeric materials and its boundary is denoted by ∂B . The internal discontinuity is approximated by the phase field.

point \mathbf{X} in the undeformed reference configuration is mapped to \mathbf{x} in the current deformed configuration. Then the deformation gradient \mathbf{F} is defined by

$$\mathbf{F} = \frac{\partial \mathbf{x}}{\partial \mathbf{X}} \quad (1)$$

The map is constrained by the condition $J = \det(\mathbf{F}) > 0$ in order to ensure non-penetrable deformations. The internal discontinuity surfaces Γ represent a set of discrete cracks. In accordance with Griffith's theory of fracture, the energy required to create a unit area of fracture surface is equal to the critical fracture energy density \mathcal{G}_c . In order to circumvent the problem associated with numerically tackling the discontinuity representing a crack, the fracture surface Γ is approximated by a phase field $p(\mathbf{X}, t)$:

$$\int_{\Gamma} \mathcal{G}_c dS = \int_B \mathcal{G}_c \left[\frac{(p-1)^2}{4\ell} + \ell \frac{\partial p}{\partial X_I} \frac{\partial p}{\partial X_I} \right] d\mathbf{X} \quad (2)$$

where ℓ is a model parameter that controls the width of the smooth approximation of the crack. The value of this phase field (p) is equal to 1 away from the crack and 0 inside the crack (refer to Fig. 1). Unless otherwise stated, we adopt the Lagrangian coordinates and all integrations are carried out in the undeformed reference configuration.

We adopt the simplest neo-Hookean model as a prototype. The present strategy can be extended to other hyperelastic materials models such as Mooney–Rivlin, Ogden or recent proposed complex hyperelastic models such as [40] and [41]. Two phase field models for the fracture of this material are adopted, and are illustrated in the following subsections.

2.1. Model M_I

In the absence of phase-field damage, the free energy density W of the neo-Hookean solid can be given by

$$W = \frac{1}{2} \mu (I_1 - 3 - 2 \ln J) + \frac{1}{2} K_B (\ln J)^2$$

where $I_1 = \text{tr}(\mathbf{F}^T \mathbf{F})$, and μ and K_B are the (initial) shear and bulk modulus respectively.

In the phase field modeling, we must take into account different behaviors of fracture in tension and compression. Here the decomposition of the free energy at finite strain is not as straightforward as that at small deformation regime. We first rewrite the free energy as

$$W = W_1 + W_2 = \frac{1}{2} \mu \sum_{i=1}^3 (\lambda_i^2 - 1 - 2 \ln \lambda_i) + \frac{1}{2} K_B (\ln J)^2 \quad (3)$$

where λ_i is the i th principal stretch, $J = \lambda_1 \lambda_2 \lambda_3$ and $I_1 = \sum_{i=1}^3 \lambda_i^2$. Here W is decomposed into $W_1 = \frac{1}{2} \mu \sum_{i=1}^3 (\lambda_i^2 - 1 - 2 \ln \lambda_i)$ and $W_2 = \frac{1}{2} K_B (\ln J)^2$. Note that W_1 is a linear function of $\ln \lambda_i$ and W_2 a nonlinear function of $\ln J$.

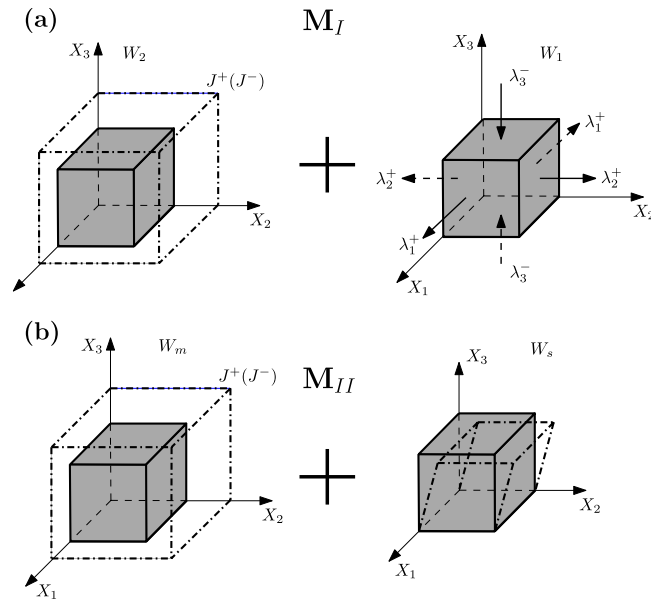


Fig. 2. The two models of energy decomposition to consider the contribution of tension and compression. (a) The current model decomposes the deformation into the volumetric and stretching parts, representing the contribution from the volumetric and stretching deformation. They are corresponding to W_2 and W_1 in Eq. (3). This model is hereafter referred to as M_I . (b) The strain energy is decomposed into the volumetric and isochoric parts, which represent the contribution from volumetric and shear deformation. Such energy decomposition (hereafter referred to as M_{II}) is adopted previously by Borden et al. [33], Arriaga et al. [42], and Arriaga and Waisman [36].

We next introduce the phase field p to model the fracture process zone. Physically it quantifies the loss of stiffness of the material in the failure zone. Inspired by Miehe et al. [19] and Borden et al. [24], we take the free energy (coupled with the phase field p) in the form

$$G_{\text{rub}} = [(1 - \mathcal{K}) p^2 + \mathcal{K}] W^+ + W^- \quad (4)$$

For intact material without damage (i.e. $p = 1$), the energy decomposition above reduces to

$$G_{\text{rub}} = W^+ + W^- = W \quad (5)$$

This is a constraint equation to be satisfied by W^+ and W^- . The former refers to the energy with tensile stretching while the latter to the energy with compression, at least in one direction.

W^+ and W^- are defined by

$$W^+ = W(\lambda_i^+, J^+) \quad \text{where } \lambda_i^+ = \begin{cases} \lambda_i & \text{for } \lambda_i > 1 \\ 1 & \text{for } \lambda_i \leq 1 \end{cases} \quad J^+ = \begin{cases} J & \text{If } J > 1 \\ 1 & \text{If } J \leq 1 \end{cases}$$

and

$$W^- = W(\lambda_i^-, J^-) \quad \text{where } \lambda_i^- = \begin{cases} \lambda_i & \text{for } \lambda_i < 1 \\ 1 & \text{for } \lambda_i \geq 1 \end{cases} \quad J^- = \begin{cases} J & \text{If } J < 1 \\ 1 & \text{If } J \geq 1 \end{cases}$$

respectively. The above phase field model is hereafter referred to as M_I . For the physical meaning of the energy decomposition, readers may refer to the schematics shown in Fig. 2a.

For demonstration, consider the two examples:

- If $\lambda_1 < 1$ and $J > 1$, we then have

$$W^+ = \frac{1}{2} \mu \sum_{i=2}^3 (\lambda_i^2 - 1 - 2 \ln \lambda_i) + \frac{1}{2} K_B (\ln J)^2, \quad W^- = \frac{1}{2} \mu (\lambda_1^2 - 1 - 2 \ln \lambda_1)$$

- If $\lambda_1 < 1$ and $J < 1$, then

$$W^+ = \frac{1}{2}\mu \sum_{i=2}^3 (\lambda_i^2 - 1 - 2 \ln \lambda_i), \quad W^- = \frac{1}{2}\mu (\lambda_1^2 - 1 - 2 \ln \lambda_1) + \frac{1}{2}K_B (\ln J)^2$$

The total potential energy of the body, U , composed of the elastic energy and the fracture energy, is given by

$$U = \int_B G_{\text{rub}} d\mathbf{X} + \int_B G_{\text{phase}}(p, \nabla p) d\mathbf{X} \quad (6)$$

with G_{phase} previously defined by the integrand in (2). The kinetic energy of the body B is

$$T = \frac{1}{2} \int_B \rho_0 \dot{x}_i \dot{x}_i d\mathbf{X} \quad (7)$$

where ρ_0 is the initial mass density. The Lagrangian for the elastic problem under study reads

$$L(\mathbf{x}, \dot{\mathbf{x}}, p) = T(\dot{\mathbf{x}}) - U(\mathbf{x}, p) = \int_B \hat{L} d\mathbf{X}$$

Variation of \hat{L} gives

$$\begin{aligned} \delta \hat{L} &= \rho_0 \dot{x}_i \delta \dot{x}_i - \frac{\partial G_{\text{rub}}}{\partial F_{iJ}} \delta x_{i,J} - \frac{\partial G_{\text{rub}}}{\partial p} \delta p - \delta G_{\text{phase}} \\ &= \frac{d}{dt} (\rho_0 \dot{x}_i \delta x_i) - \left(\frac{\partial G_{\text{rub}}}{\partial F_{iJ}} \delta x_i \right)_{,J} - \frac{\partial G_{\text{rub}}}{\partial p} \delta p + \left[\left(\frac{\partial G_{\text{rub}}}{\partial F_{iJ}} \right)_{,J} - \rho_0 \ddot{x}_i \right] \delta x_i - \delta G_{\text{phase}} \end{aligned} \quad (8)$$

where

$$\frac{\partial G_{\text{rub}}}{\partial p} = 2(1 - \mathcal{K}) p W^+.$$

The first Piola–Kirchhoff stress with damage can be obtained

$$P_{iJ} = \frac{\partial G_{\text{rub}}}{\partial F_{iJ}} = [(1 - \mathcal{K}) p^2 + \mathcal{K}] \frac{\partial W^+}{\partial F_{iJ}} + \frac{\partial W^-}{\partial F_{iJ}} \quad (9)$$

where

$$\frac{\partial W^+}{\partial F_{iJ}} = \sum_{k=1}^3 \frac{\partial W^+}{\partial \lambda_k^+} \frac{\partial \lambda_k^+}{\partial F_{iJ}} + \frac{\partial W^+}{\partial J^+} \frac{\partial J^+}{\partial F_{iJ}}, \quad \frac{\partial W^-}{\partial F_{iJ}} = \sum_{k=1}^3 \frac{\partial W^-}{\partial \lambda_k^-} \frac{\partial \lambda_k^-}{\partial F_{iJ}} + \frac{\partial W^-}{\partial J^-} \frac{\partial J^-}{\partial F_{iJ}}$$

with

$$\begin{aligned} \frac{\partial \lambda_k^+}{\partial F_{iJ}} &= \begin{cases} \frac{\partial \lambda_k}{\partial F_{iJ}} & \text{for } \lambda_k > 1 \\ 0 & \text{for } \lambda_k \leq 1 \end{cases}, \quad \frac{\partial \lambda_k^-}{\partial F_{iJ}} = \begin{cases} \frac{\partial \lambda_k}{\partial F_{iJ}} & \text{for } \lambda_k < 1 \\ 0 & \text{for } \lambda_k \geq 1 \end{cases} \\ \frac{\partial J^+}{\partial F_{iJ}} &= \begin{cases} \frac{\partial J}{\partial F_{iJ}} & \text{for } J > 1 \\ 0 & \text{for } J \leq 1 \end{cases}, \quad \frac{\partial J^-}{\partial F_{iJ}} = \begin{cases} \frac{\partial J}{\partial F_{iJ}} & \text{for } J < 1 \\ 0 & \text{for } J \geq 1 \end{cases} \end{aligned}$$

and

$$\delta G_{\text{phase}} = \frac{\partial G_{\text{phase}}}{\partial p} \delta p = \left(2\ell \mathcal{G}_c \frac{\partial p}{\partial X_I} \delta p \right)_{,I} + \left(\mathcal{G}_c \frac{p-1}{2\ell} - 2\ell \mathcal{G}_c \frac{\partial^2 p}{\partial X_I^2} \right) \delta p$$

Setting $\delta L = 0$ leads to

$$\frac{\partial P_{iJ}}{\partial X_J} = \rho_0 \ddot{x}_i, \quad (10)$$

$$[4\ell(1 - \mathcal{K}) W^+ + \mathcal{G}_c] p - 4\mathcal{G}_c \ell^2 \frac{\partial^2 p}{\partial X_I^2} = \mathcal{G}_c, \quad (11)$$

with natural boundary conditions

$$p_{,I} N_I = 0 \quad (12)$$

$$P_{iJ}N_J = t_i \quad (13)$$

where t_i is the traction prescribed on the outer surface ∂B with the normal vector N .

For the proposed model M_I , a Bourdin-type phase field theory is adopted. The phase field is solved by Eq. (11). The time evolution of phase field is not necessary. But it is required by Ginzburg–Landau theory.

2.2. Model M_{II}

The phase field model M_I is different from the ones proposed by Amor et al. [37] and Borden et al. [24] for small-strain regime and Borden et al. [33] and Arriaga and Waisman [36] for finite-strain elasticity. For comparison, we follow their approaches to establish another phase field model, in which the elastic energy is separated into isochoric and volumetric parts. For the neo-Hookean solid under consideration, the strain energy takes the form

$$W = W_s(\bar{I}_1) + W_m(J) \quad (14)$$

where W_s is only the function of $\bar{I}_1 = J^{-2/3}I_1$:

$$W_s = \frac{1}{2}\mu(\bar{I}_1 - 3) \quad (15)$$

and W_m is just the function of J :

$$W_m = \frac{1}{2}K_B \ln(J)^2 \quad (16)$$

The phase-field coupled free energy can be defined as

$$G_{\text{rub}}(\bar{I}, J, p) = [(1 - \mathcal{K})p^2 + \mathcal{K}][W_s(\bar{I}) + W_m^+(J)] + W_m^-(J) \quad (17)$$

where $W_m^\pm = W_m H^\pm$,

$$H^+ = \begin{cases} 1, & \text{for } \frac{\partial W}{\partial J} \geq 0 \\ 0, & \text{for } \frac{\partial W}{\partial J} < 0 \end{cases}$$

and

$$H^- = \begin{cases} 0, & \text{for } \frac{\partial W}{\partial J} \geq 0 \\ 1, & \text{for } \frac{\partial W}{\partial J} < 0 \end{cases}$$

The sign of H^\pm depends on whether the material is under hydrostatic tension or compression. Likewise, readers may refer to the schematics shown in Fig. 2b for the physical meaning of the energy decomposition.

It can be shown that the mean (hydrostatic) part of the Cauchy stress σ in the absence of the phase field damage is just

$$\sigma_m = \frac{1}{3} \frac{\partial W}{\partial J}$$

This equation is obtained directly by the definition of Cauchy stress σ . Following the same variational approach as shown before, we can derive similar governing equations and the associated initial boundary conditions. For later comparison, we refer to this model as M_{II} . It should be commented here that although we follow Amor et al. [37] in which the phase field model is formulated at the small deformation regime, the M_{II} method is implemented under the finite deformation framework, illustrated above.

Remark 1. Under generalized plane deformations, Eq. (9) in M_I can be greatly simplified. Consider for instance the deformation gradient tensor

$$\mathbf{F} = \begin{pmatrix} s_1 & \kappa_1 & 0 \\ \kappa_2 & s_2 & 0 \\ 0 & 0 & s_3 \end{pmatrix}$$

Following the polar decomposition ($\mathbf{F} = \mathbf{R}\mathbf{U} = \mathbf{V}\mathbf{R}$) in [43], the right stretch \mathbf{U} can be found in an explicit form as

$$\mathbf{U} = \begin{pmatrix} \frac{s_1(s_1 + s_2) - \kappa_2(\kappa_1 - \kappa_2)}{\sqrt{(s_1 + s_2)^2 + (\kappa_1 - \kappa_2)^2}} & \frac{\kappa_1 s_1 + \kappa_2 s_2}{\sqrt{(s_1 + s_2)^2 + (\kappa_1 - \kappa_2)^2}} & 0 \\ \frac{\kappa_1 s_1 + \kappa_2 s_2}{\sqrt{(s_1 + s_2)^2 + (\kappa_1 - \kappa_2)^2}} & \frac{s_2(s_1 + s_2) + \kappa_1(\kappa_1 - \kappa_2)}{\sqrt{(s_1 + s_2)^2 + (\kappa_1 - \kappa_2)^2}} & 0 \\ 0 & 0 & s_3 \end{pmatrix}$$

with the three principal (stretches) eigenvalues

$$\begin{aligned} \lambda_1 &= \frac{1}{2} \left(\sqrt{(\kappa_1 - \kappa_2)^2 + (s_1 + s_2)^2} - \sqrt{(\kappa_1 + \kappa_2)^2 + (s_1 - s_2)^2} \right) \\ \lambda_2 &= \frac{1}{2} \left(\sqrt{(\kappa_1 - \kappa_2)^2 + (s_1 + s_2)^2} + \sqrt{(\kappa_1 + \kappa_2)^2 + (s_1 - s_2)^2} \right) \\ \lambda_3 &= s_3 \end{aligned}$$

The principal stretches are functions of the component of deformation gradient tensor F_{ij} . Hence it is straightforward to derive the stress with the phase-field damage (9) as well as the associated variational formulation.

Remark 2. For the convenience of three-dimensional numerical implementation, the right Cauchy–Green tensor is defined as

$$\mathbf{C} = \mathbf{F}^T \mathbf{F} = \mathbf{U}^2 = \mathbf{Q} \mathbf{\Lambda} \mathbf{Q}^T$$

where \mathbf{Q} consists of the orthogonal eigenvectors of \mathbf{C} and $\mathbf{\Lambda} = \text{diag}(\lambda_1^2, \lambda_2^2, \lambda_3^2)$ is a diagonal matrix of the eigenvalues of the right Cauchy–Green tensor. Because \mathbf{C} is symmetric, it is easy to derive the stress and tangent modulus [44].

Remark 3. It has been mentioned in [33] that the spectral decomposition of a logarithmic strain tensor can be used for the phase-field modeling of fracture at finite strain. The logarithmic strain tensor can be decomposed into tensile and compressive parts (see Eqs. 58–61 therein). With the decomposition of logarithmic strain tensor, the deformation energy is expressed by a hypoelastic relationship. However, it is mentioned that this strategy is limited to certain brittle fracture simulations, and not adopted in their work. On the other hand, the hypoelastic relationship cannot reflect the hyperelastic property of the material. The present decomposition is also different from the multiplicative split of the principal stretches proposed by Hesch and Weinberg [38] for finite deformation.

Remark 4. It should be noted that \mathcal{K} is a model parameter ($\ll 1$) introduced to achieve better numerical stability. For linear elastic materials, introduction of \mathcal{K} has shown to be unnecessary by Borden et al. [24]. For non-linearly elastic solids, however, our numerical experiments suggest the introduction of a non-zero \mathcal{K} .

Remark 5. We apply the staggered scheme to solve the evolution equations of fracture. The staggered algorithm is summarized in Box I. At a given time step, the momentum equation is solved first to update the displacement. With the updated displacements, the phase field is solved. The stagger scheme can reduce the original problem to two smaller systems. It is more flexible and stable numerically.

3. Numerical examples

We now demonstrate the modeling capability of the current approach to predict the fracture of rubber-like material at finite deformation. To make contact with the approaches by Borden et al. [33] and Arriaga et al. [42] as M_{II} , we present our model prediction (M_I) against M_{II} . All simulations shown in this section are carried out by standard C^0 finite elements. Simulation cases are identified by C1, C2, C3 and C4 for ease of illustration.

1. Initialization. The displacements and fracture phase fields of the previous step \mathbf{u}_{i-1} , p_{i-1} are known.

$$(\mathbf{u}_{old}, p_{old}) = (\mathbf{u}_{i-1}, p_{i-1})$$

2. Compute displacement field. Determine the current displacement \mathbf{u}_{new} at frozen fracture phase field p_{old} to solve the equation below.

$$\int_B P_{iJ} \frac{\partial \delta x_i}{\partial X_J} d\mathbf{X} - \int_{\partial B} P_{iJ} N_J \delta x_i dS = 0$$

with the first P-K stress

$$P_{iJ} = [(1 - \mathcal{K}) p_{old}^2 + \mathcal{K}] \frac{\partial W^+(\mathbf{u}_{new})}{\partial F_{iJ}} + \frac{\partial W^-(\mathbf{u}_{new})}{\partial F_{iJ}}$$

3. Compute Fracture Phase Field. Determine the current fracture phase field p_{new} to solve the equation below.

$$\int_B \{ (1 - \mathcal{K}) 2p_{new} W^+(\mathbf{u}_{new}) \delta p + \frac{\mathcal{G}_c (p_{new} - 1) \delta p}{2l_0} + 2\mathcal{G}_c l_0 \frac{\partial \delta p}{\partial X_I} \frac{\partial p_{new}}{\partial X_I} \} d\mathbf{X} = 0$$

4. Convergence test

$$\text{if } \|p_{new} - p_{old}\|_{\infty} > tol \text{ repeat 2-4, } p_{old} = p_{new}.$$

5. Update the displacements and phase fields

$$(\mathbf{u}_i, p_i) = (\mathbf{u}_{new}, p_{new}), p_i \leq p_{i-1}$$

Box I. Staggered scheme for phase field fracture.

3.1. Uniaxial tension of a square block

In this subsection, we consider displacement-controlled quasi-static tensile loading imposed on a square block, which serves as a benchmark to compare our method and the one adopted by Borden et al. [33] and Arriaga et al. [42]. The geometry and boundary conditions are given in Fig. 3a. The plane-strain condition is assumed. Values of the Young's modulus and Poisson's ratio taken in the analyses are $E = 14.5$ MPa and $\nu = 0.385$. The shear modulus and bulk modulus can be obtained through a classical relationship. The length scale is set as $\ell/L = 0.04$ and the fracture energy density is $\mathcal{G}_c = 1.5$ N/mm. There is no pre-set crack in the model. The linear triangle element is used in these simulations. The total number of elements and nodes for the FE model are around 5000 and 2601, following the mesh convergence study.

Fig. 3b shows the load–displacement curves calculated from the aforementioned two models. As can be seen from Fig. 3, although there is somewhat difference, the results obtained from the current model (M_I) are in fairly good agreement with those from M_{II} as previously adopted by Borden et al. [33], Arriaga et al. [42] and Arriaga and Waisman [36]. Both models predict almost the same maximum load at almost the same displacement. After the peak the crack phase field develops very fast and leads to a rapid drop of the force.

Fig. 4 shows the progression of the crack phase field at several different load levels. The square block deforms with a certain necking at $u = 0.7$ mm (see Fig. 4(a1) and (b1)), at which no visible phase field is observed. When the imposed displacement u/L is about 0.81, the phase field develops around the localized necking (Fig. 4(a2) and (b2)). The crack phase field by M_I is more concentrated than that by M_{II} . In other words, the model M_{II} predicts more diffusive necking than M_I . As illustrated in Fig. 4(a3) and (b3), a little increase of the outer imposed displacement leads to complete failure of the samples. For the purpose of illustration, the material elements with the crack phase field less than 0.05 are removed from the displayed images. Let the complete failure of the material be represented by the phase field $p < 0.05$. We can see that M_I can predict the formation of a sharp crack. On the contrary, the prediction of M_{II} is more like a V-shaped crack. This V-shaped crack surface is seldom observed in real experiments.

For comparison, we carried out a uniaxial tensile test on a hydrogel plate (i.e., a rubbery-like elastic solid). The fracture surface observed through the broken specimen is shown to be flat (see the inset in Fig. 4), which is in good agreement with that predicted by M_I . Although the example shown in Fig. 4 is simple, it gives an insight into the

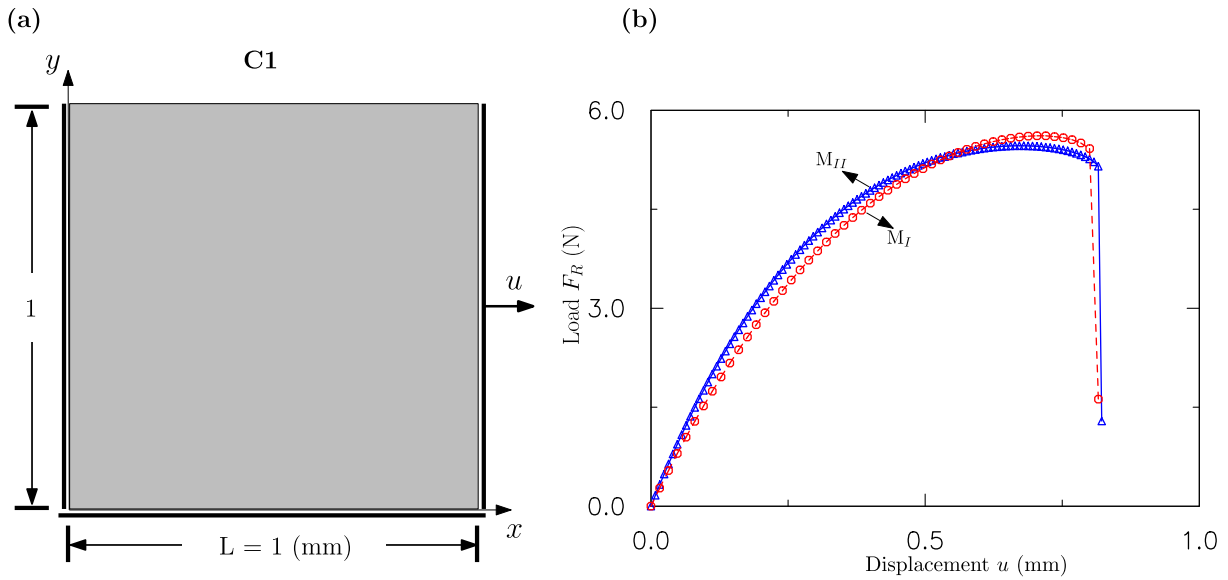


Fig. 3. Two model predictions for uniaxial tension of a square block. (a) Geometry and boundary conditions and (b) load vs. displacement curves simulated with the same geometry, boundary condition, and material parameters.

performance of the proposed two models. The possible reason that the energy decomposition in M_I is better than M_{II} is that the energy decomposition in M_{II} distinguishes bulk compressions rather than fiber compressions — possible distinct compressions among the three principal stretches. This point has been illustrated in Fig. 2a. To be more specific, if $J = \lambda_3^- \lambda_1^+ \lambda_2^+$ is less than 1, the material is judged by M_{II} as to be in a state of compression. Here only shear deformation can contribute to the formation of crack. In realistic physical process, the tensile stretches λ_1^+ and λ_2^+ can also contribute to the fracture, as have been taken into account by M_I , but ignored by M_{II} .

3.2. Penny shaped pre-cracked test specimen

In this section, we consider a displacement-controlled quasi-static benchmark test from [34]. A rectangular plate of 2 mm width and 0.4 mm height with a horizontal pre-notch of 0.2 mm length at the center under the tensile loading is investigated. The geometric setup is shown in Fig. 5a. In order to capture the crack pattern properly, the mesh is refined around the pre-notch. The finite element mesh includes 9459 elements with the minimum element size 0.0057 mm and 4888 nodes, following the mesh convergence study. The shear modulus is chosen as $\mu = 5.2$ MPa and a weakly compressible response is considered with Poisson's ratio $\nu = 0.385$. The fracture energy is set to $\mathcal{G}_c = 1.5$ N/mm. A monotonic displacement is imposed on the top surface with the constant displacement increment $\Delta u = 0.0016$ mm and the bottom is fixed in the y direction. Fig. 5b shows the load–displacement curves calculated from the aforementioned two models. The general response is very similar to those shown in Fig. 9 of [34] therein. It can be seen from Fig. 5 that the force–displacement response predicted by M_I is almost the same as that of M_{II} at the initial stage of the deformation. However, the corresponding displacement where the force drops by M_I is smaller than that by M_{II} . It means that the initiation of fracture is a little retarded as predicted by M_{II} . It can be seen from Fig. 5 that the response of the specimen predicted by M_{II} cannot go into the softening stage but M_I can, which is expected to occur during the crack propagation. It is implied that M_I is more robust numerically than M_{II} .

Fig. 6 shows the current deformed specimen at different levels of the imposed displacement. Up to the imposed displacement $u = 0.37$ mm, the specimen has experienced large deformation but the fracture phase field is virtually undeveloped (see Fig. 6a). At the applied displacement $u = 0.41$ mm, however, we observe that the phase field begins to develop in the area close to point A (see Fig. 6b). It is intuitively consistent with the fact that high stress concentration around the point will induce high damage. For an imposed deformation of $u = 0.42$ mm, the fracture phase field is fully developed in the vicinity of the horizontal notch (Fig. 6c). A rapid cracking occurs when the fracture phase field has reached a threshold, resulting in the full damage (see Fig. 6d). In comparison with [34] (see Fig. 10

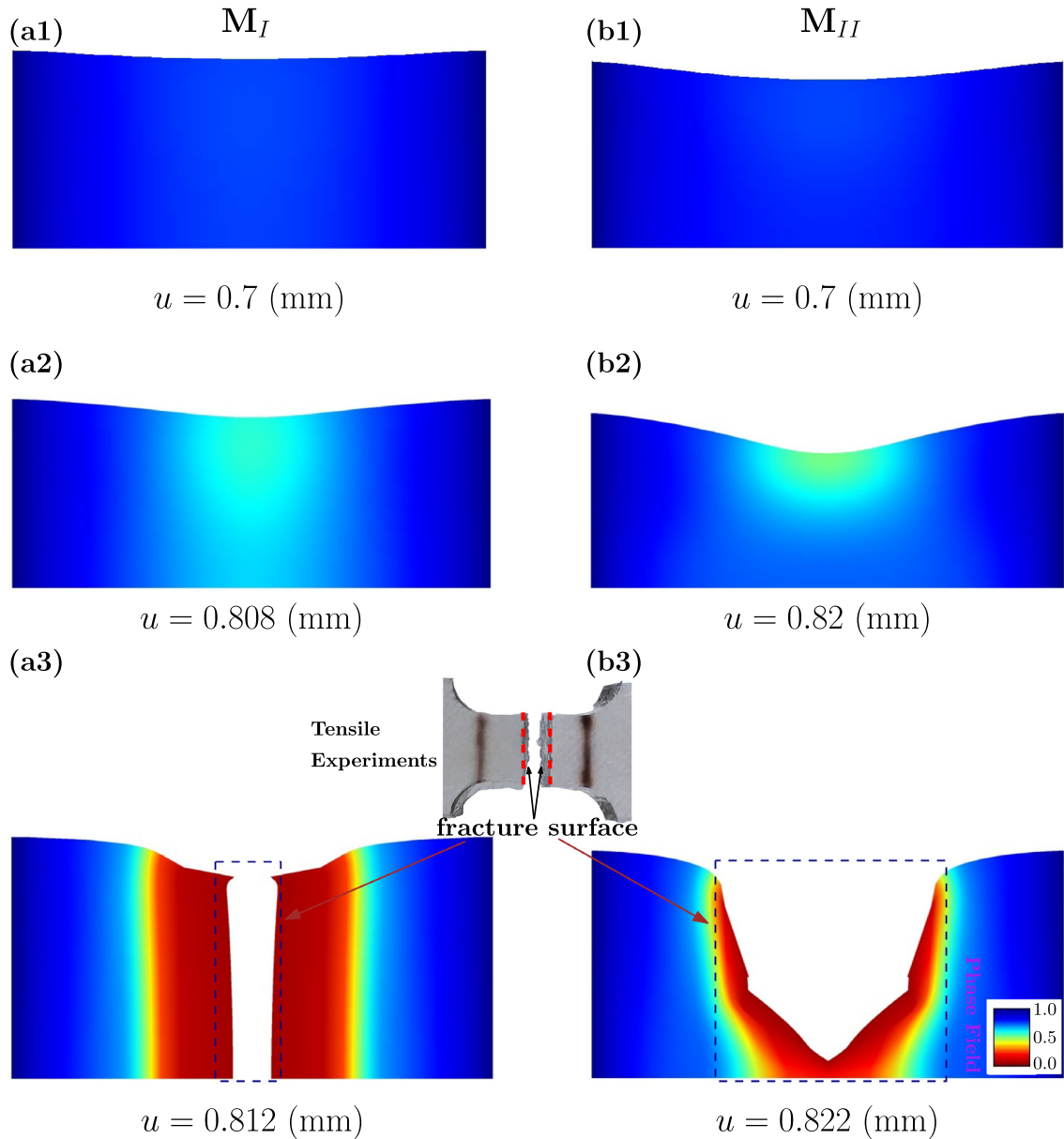


Fig. 4. The phase field of cracking of a square block under different levels of remote tension. (a1)–(a3) from M_I ; (b1)–(b3) from M_{II} as previously adopted by Borden et al. [33], Arriaga et al. [42], and Arriaga and Waisman [36]. The fractured specimen of hydrogel under tensile loading is shown as inset.

therein), the initial large deformation process predicted by M_I looks similar. However, the present model predicts that the crack propagates perpendicular to the loading direction more like a forward arrow, which is in sharp contrast with the two parallel lines in their work. The crack propagates and fracture occurs in a very short time though the outer imposed displacement has only a tiny increment.

The contours of the nominal stress P_{yy} and the fracture phase fields are demonstrated in Fig. 7a and b respectively at the imposed displacement level $u = 0.42$ mm. Although the fracture phase field is shown in Fig. 6, we further zoom in the region around the notch to observe it more closely. It can be seen that the stress P_{yy} around the notch is almost zero in Fig. 7a, which means the initiation of crack propagation. For the visualization purpose of the fracture phase field, we have removed the elements over which the fracture phase field p is less than or equal to 0.05. As shown in

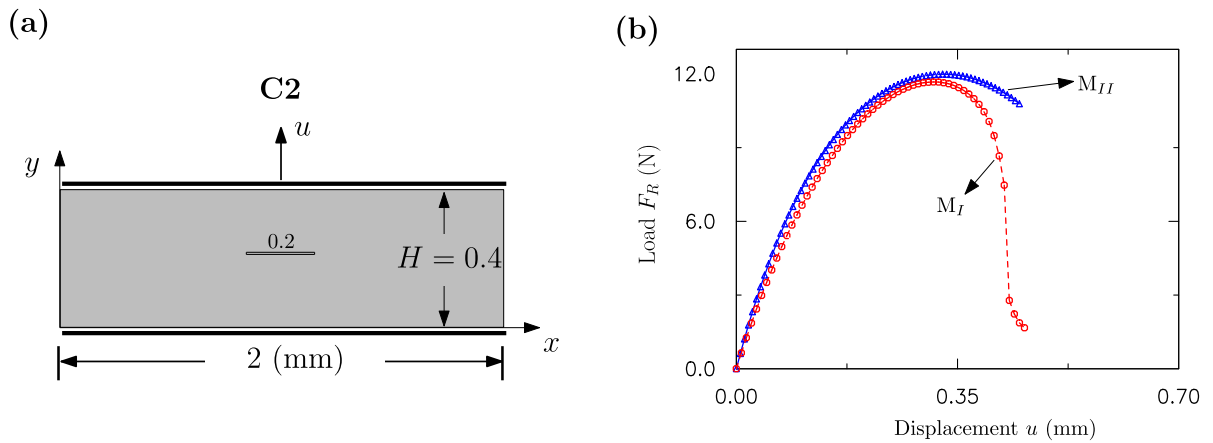


Fig. 5. Fracture of a rectangular plate with a centered pre-set notch under remote tension u . (a) Geometry and boundary conditions and (b) model prediction of load–displacement curves by M_I and M_{II} .

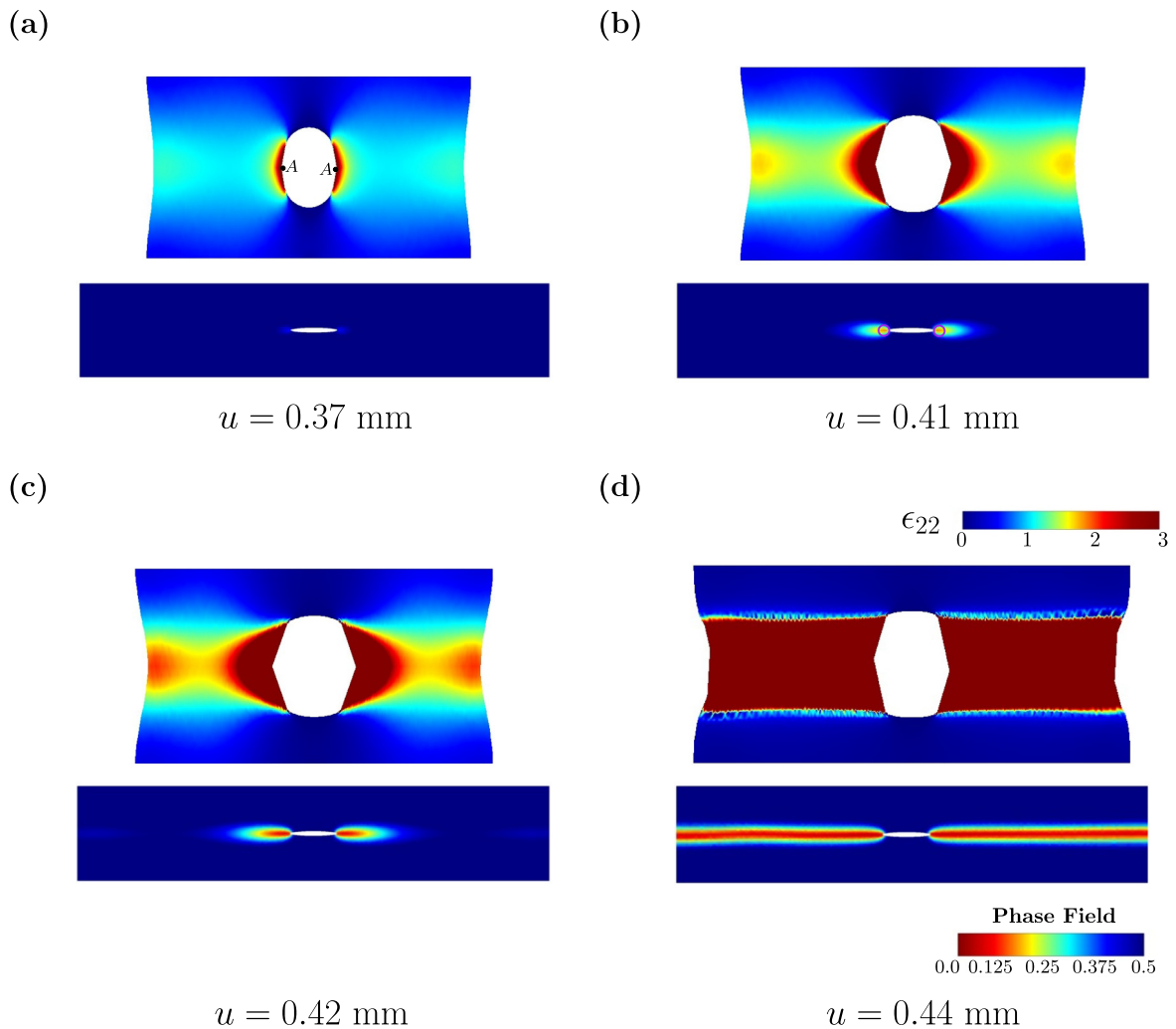


Fig. 6. The phase field around the notch in the current deformed and undeformed reference configurations respectively, under different levels of imposed displacement: (a) $u = 0.37$ mm; (b) $u = 0.41$ mm; (c) $u = 0.42$ mm; (d) $u = 0.44$ mm. The current approach (M_I) is used here.

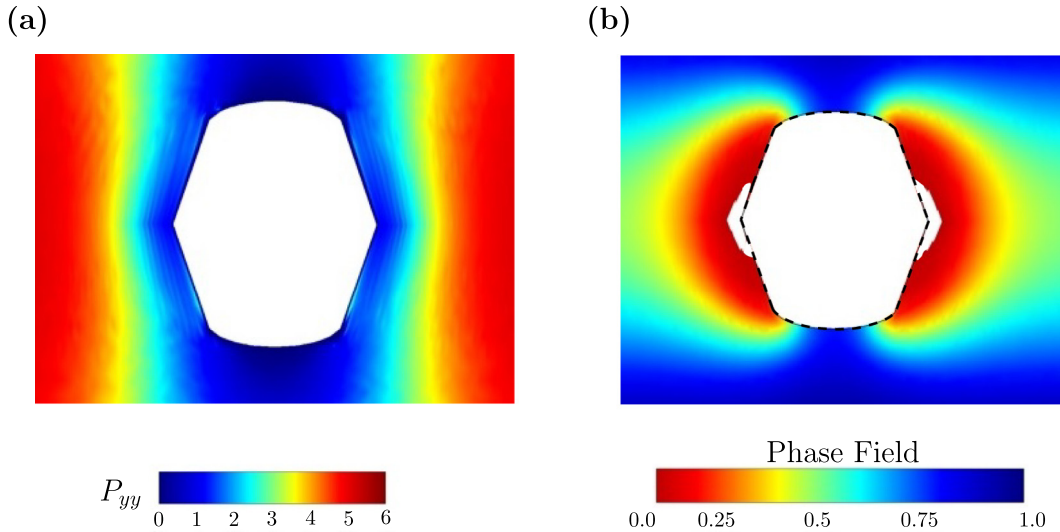


Fig. 7. The zoom-in contour plot of (a) the nominal stress P_{yy} and (b) the phase field around the notch at the imposed displacement $u = 0.42$ mm.

Fig. 7b, the contour plot of the fracture phase field is adapted for comparison with Fig. 6 where the fracture phase field with $p \leq 0.05$ is not displayed. Similar to [34], the real boundary of the notch is shown with the dashed lines. In comparison with [34], the fracture predicted by M_I is more localized at the region with high stress concentration. However, the result shown by Miehe and Schänzel [34] has a more diffusive damage around the notch along the loading direction. It appears that distinguishing the contribution of tension and compression in free energy can lead to the more localized fracture process zone.

Fig. 8 shows the deformed specimen at the different levels of the imposed displacement using the model M_{II} . Generally speaking, the deformation of the pre-notch is very similar to what is observed by using M_I . Significant difference between the two model predictions lies in the fact that the strain around the deformed notch is not as smooth as the one shown in Fig. 6. Thus M_{II} may lead to earlier termination of computation where the fracture phase field is not fully developed. This is in a good agreement with that shown in Fig. 5b where the expected stress drop is not observed.

3.3. Double edge notched specimen in tension

Following [34], we are trying to reproduce the experimental results of Hocine et al. [45]. They have performed the experiments on double edge notch tension specimens. All of their specimens have an initial notch with different sizes. The geometry setup is shown in Fig. 9a. The initial crack length varies and has the initial values $a_i = \{12, 20, 28\}$ mm. Due to the symmetry of the specimen, only one quarter of the specimen is needed to model, which is discretized by approximately 30000 elements. The meshes are refined around the initial notch. Compared to [34], we have used more elements herein. The minimum size of elements is 0.66 mm. The dimension of length used in our simulations is 1.5 mm, comparable to the size of 2 elements. The imposed displacement is increased in a monotonic way. The material parameters used here are consistent with [34]: the shear modulus is 0.19 MPa and the Poisson's ratio 0.45. The fracture energy is $\mathcal{G}_c = 1.5$ N/mm.

Fig. 9b shows the load vs. displacement obtained from the experiments for the three specimen geometries. The lines without symbol represent the results measured from the experiments by Hocine et al. [45] while the lines with symbol represent the simulation results predicted by our model M_I . As anticipated, the longer the notch, the lower the maximum fracture force. The specimen with the largest initial notch $a = 28$ mm results in the lowest fracture force level. It can be seen from Fig. 9b that the numerical simulations agree with the experimental results in a reasonable way. When the maximum load is reached, the crack propagates rapidly and the stress has a sudden drop.

Fig. 10 plots the deformed configuration with the smallest initial notch $a = 12$ mm. The crack initiation and growth are visualized by harnessing the level set function. The removal of the continua which has the negligible stiffness is

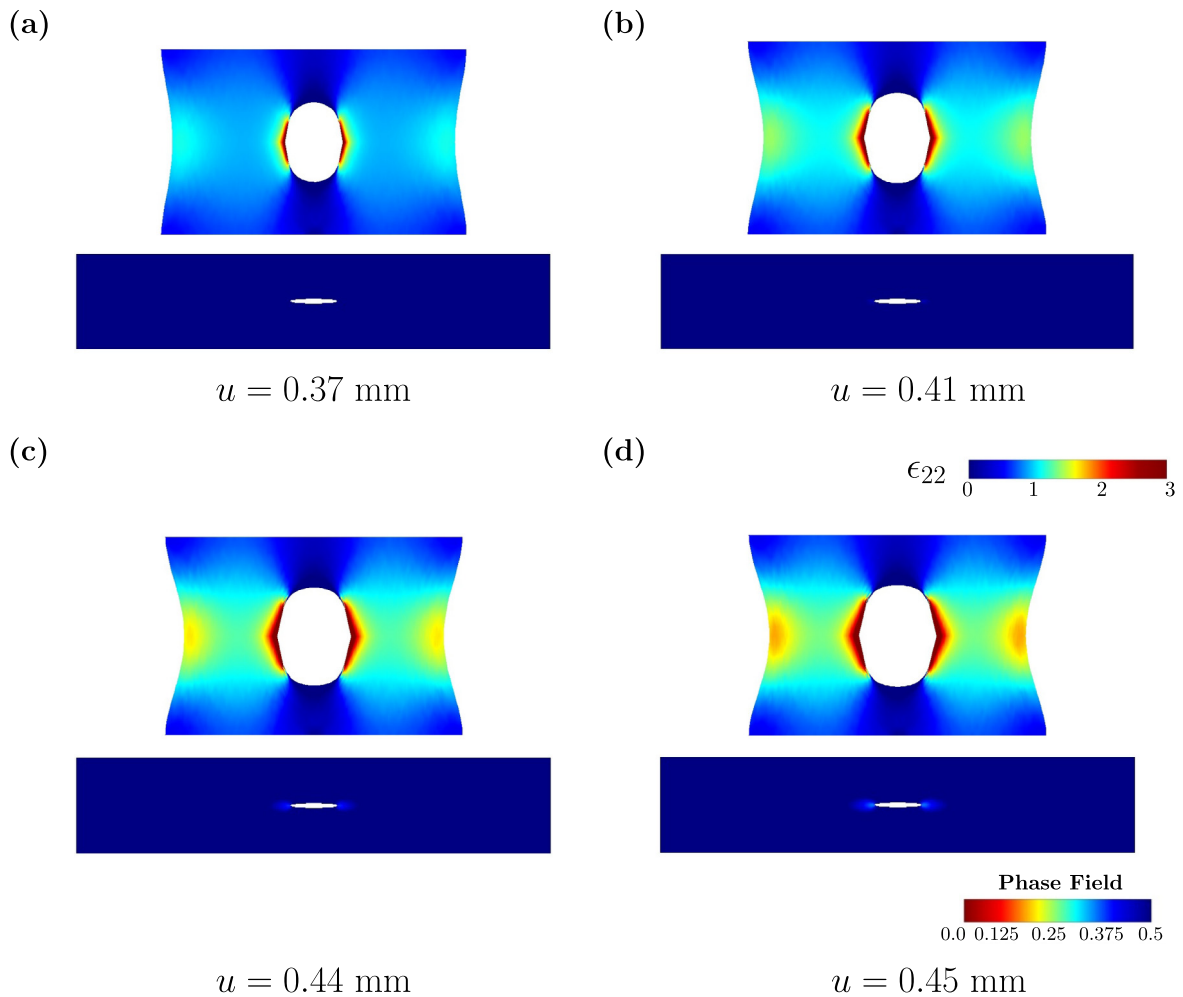


Fig. 8. The phase field around the notch in the current deformed and undeformed reference configurations respectively, under different levels of imposed displacement: (a) $u = 0.37$ mm; (b) $u = 0.41$ mm; (c) $u = 0.44$ mm; (d) $u = 0.45$ mm. The model M_{II} is used here.

chosen at a level set of $p \leq 0.05$. The contour plot of the phase field is adapted such that the area satisfying the condition is not displayed. In comparison of our results with [34] (see Fig. 13 therein), we see that Fig. 10a–c are very similar to their results. Here the final fast failure process is not shown clearly by the present simulation because viscous regularization is not introduced. Although this difference is existing, the broken specimen shown in their results is almost the same as that predicted by ours. Although not shown here, M_I is more robust numerically than M_{II} to fit the experiments.

3.4. Three-point bending test

In the previous examples, only the uniaxial tension load is involved, where the fracture only undergoes the tensile stress. The effect of existing both tension and compression on the fracture is not demonstrated. Then we finally consider three-point bending of a block containing a straight vertical notch in which both tension and compression are involved. The geometry of the model, boundary conditions and mesh of the problem is shown in Fig. 11. The FE mesh is composed of 15412 elements and 7901 nodes respectively, following the mesh convergence study. Computations are performed in a displacement-driven context. Both the x and y degree-of-freedom at the two supports are fixed. The parameters used in our simulations are also given in Table 1.

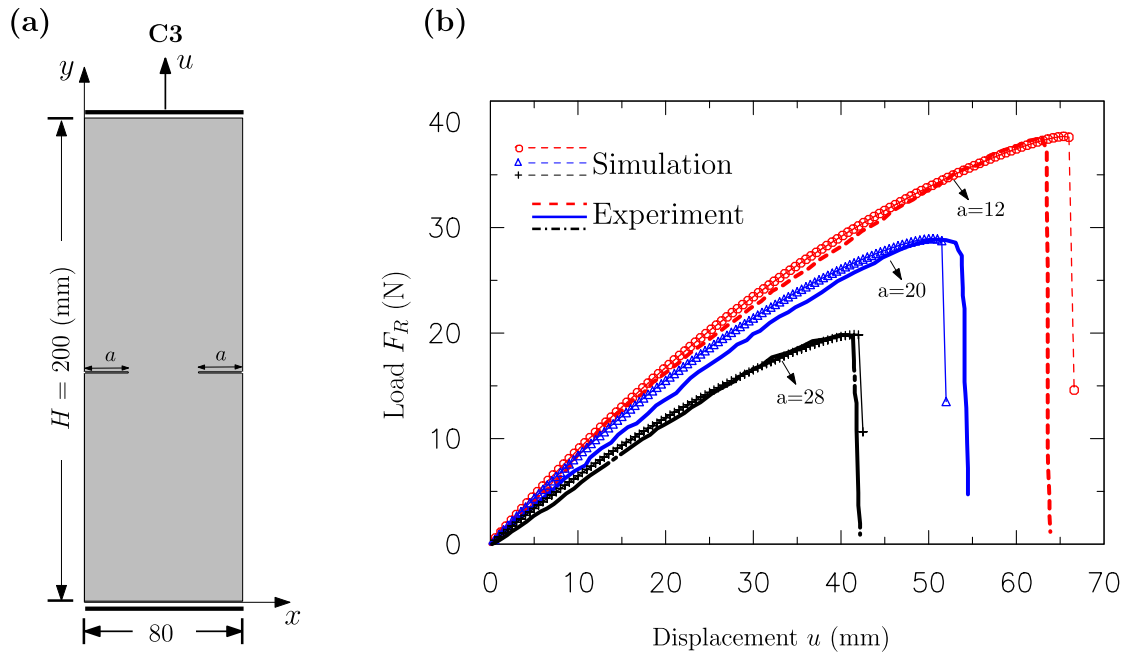


Fig. 9. Fracture of double edge notched specimen under remote tension. (a) Geometry and boundary conditions and (b) model prediction vs. experiment of load–displacement curves for three different initial notch sizes: $a = 12, 20, 28$ mm.

Table 1

Values of the parameters used in the simulations.

	μ	ν	\mathcal{G}_c	ℓ
C1	5.2 Mpa	0.385	1.5 N/mm	0.04 mm
C2	5.2 Mpa	0.385	1.5 N/mm	0.04 mm
C3	0.19 Mpa	0.45	1.5 N/mm	1.5 mm
C4	1.86 Mpa	0.45	0.075 N/mm	0.02 mm

Fig. 12 shows the stress contour P_{xx} of the deformed configuration under the four levels imposed displacement, i.e., $d/H = 0.5, 0.73, 0.9, 1.0$, as marked in the figure respectively. The contour plots of the phase field are shown. The material in the top region of the block is compressed while is stretched at the bottom. From the contour of crack phase field, it can be seen that the crack propagates along a straight line towards the top surface and the phase field is localized. The stress fields around the crack tip are concentrated. These concentrated stress fields move with the crack tip as the crack propagates. Outside the crack region, the stress is more uniform.

4. Conclusion

This paper has presented a novel energy decomposition that considers the distinct contribution of tension and compression in the phase field modeling of crack initiation and growth within the framework of finite deformation. The elastic energy (which is well accepted for a nonlinearly elastic solid) has been rewritten in terms of stretching and volumetric parts. The two parts are summed to be strictly equal to the total elastic energy for the intact material. The energy decomposition is then integrated into the Bourdin-type phase field formulation since the Griffith's theory is well understood and used in many engineering applications. Compared with the decomposition into isochoric and volumetric parts, the proposed energy decomposition is more consistent with the physical picture, as elucidated in the three representative examples.

The Lagrangian for the phase field modeling of fracture has been formulated in terms of displacement and phase fields. The resulting coupled system of equations is solved by a staggering scheme. We have verified the model

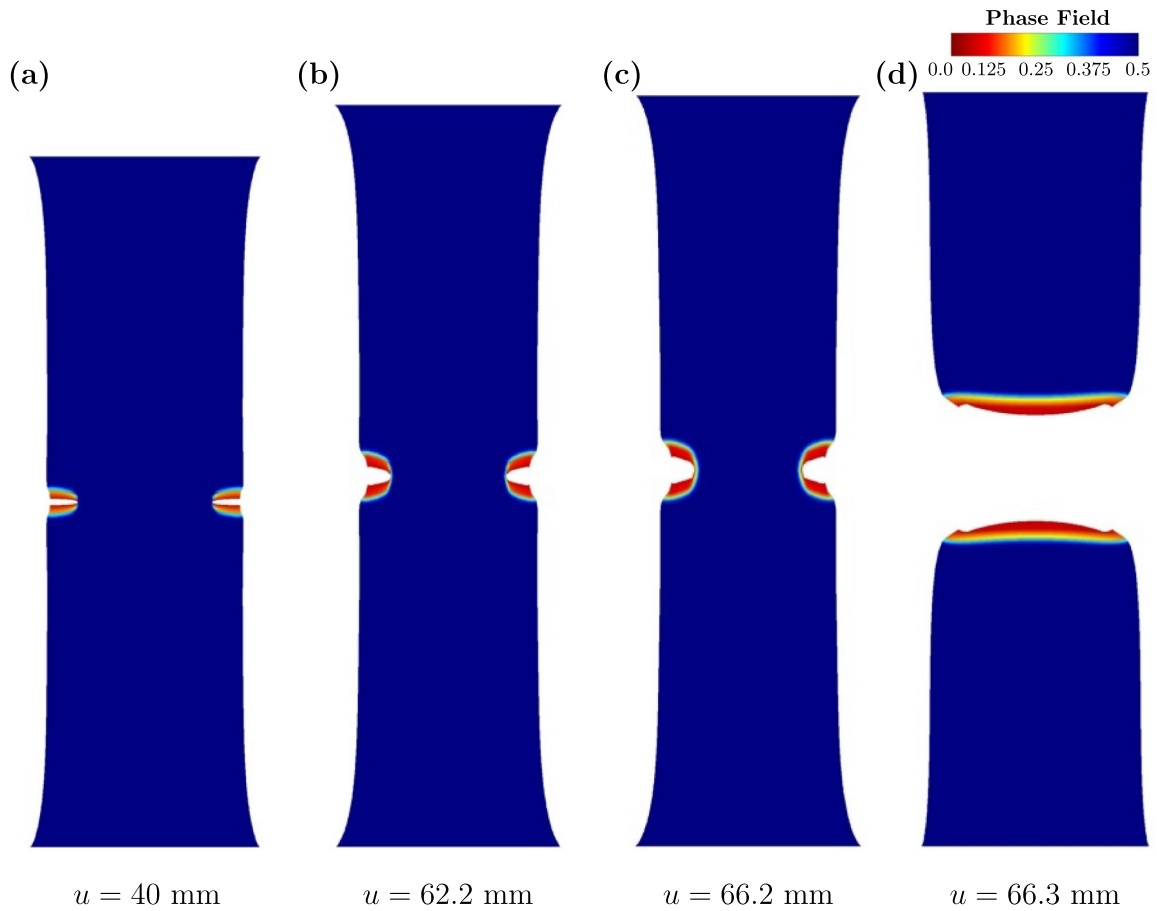


Fig. 10. The phase field of cracking of an initially double edge notched specimen in the current deformed configuration under different levels of imposed displacement: (a) $u = 40$ mm; (b) $u = 62.2$ mm; (c) $u = 66.2$ mm; (d) $u = 66.3$ mm, predicted by M_I .

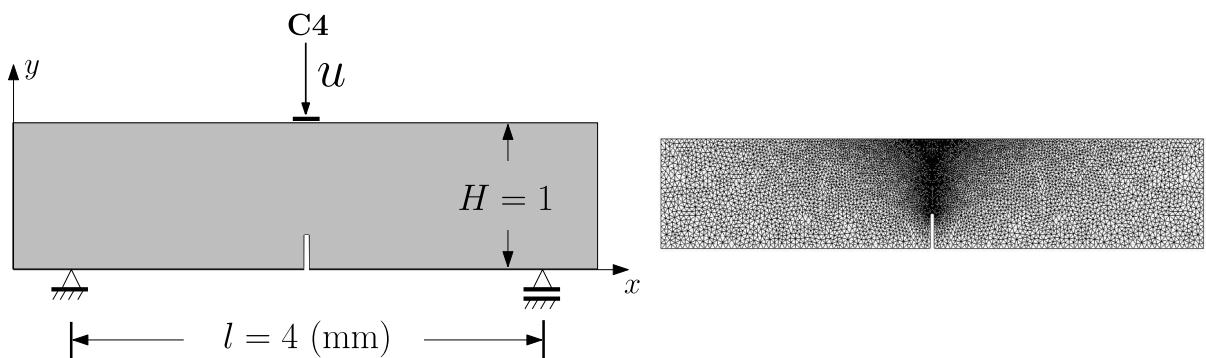


Fig. 11. Geometry, boundary conditions and FE mesh of three-point bending simulations.

predictions through several numerical experiments for crack initiation and propagation. The numerical examples show that the predicted fracture surfaces agree well with those observed in experimental tests. The proposed model is more robust than the existing models in literature. Specifically, the present model can predict the fracture of a double-edge specimen reasonably.

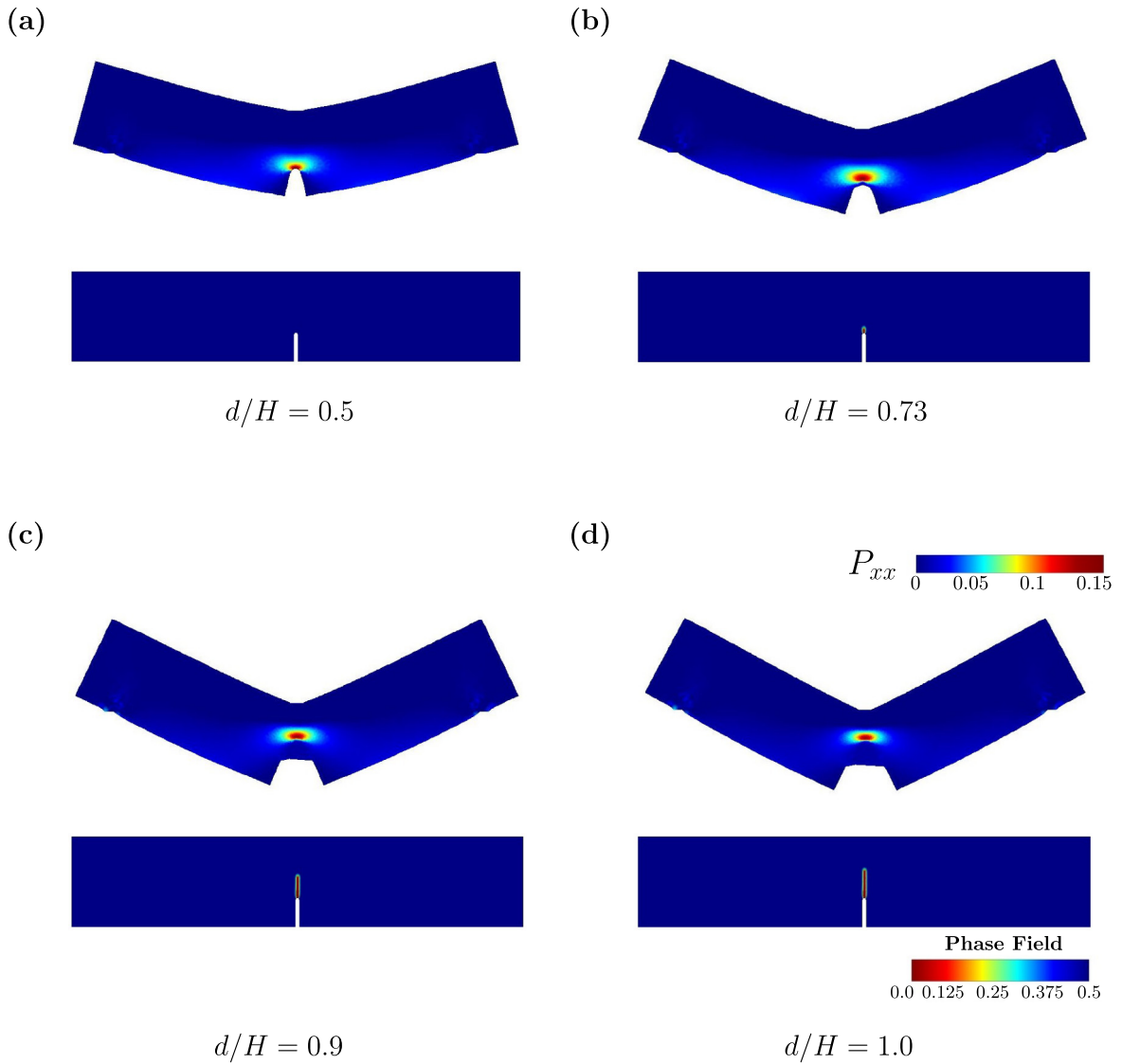


Fig. 12. The phase field of cracking of a three-point bending in the current deformed and undeformed reference configurations respectively, under different levels of imposed displacement: (a) $d/H = 0.5$; (b) $d/H = 0.73$; (c) $d/H = 0.9$; (d) $d/H = 1.0$. The model M_I is employed here. The material parameters are given in Table 1.

As the energy has been shown to be split into two parts — principal stretches and volumetric deformation respectively, the degree of tension–compression asymmetry can be considered by setting different coefficients in different parts. In contrast, the asymmetry behavior is not easy to be incorporated in [33,36]. Hence the present model can be extended to simulate the fracture of rubber-like polymeric materials with certain tension–compression asymmetry. Moreover, in viewing that most biomaterials exhibit the tension–compression asymmetry, the proposed model opens a new avenue for modeling the fracture of many biomaterials. These are the focus of our future work.

Acknowledgments

S.T. appreciates the support from NSF of China (Project No. 11872139). X.G. Thanks the support from NSF of China (11732004, 11821202), and Program for Changjiang Scholars, Innovative Research Team in University (PCSIRT).

References

- [1] K.I. Jang, H.U. Chung, S. Xu, C.H. Lee, H. Luan, J. Jeong, H. Cheng, G.T. Kim, S.Y. Han, J.W. Lee, et al., Soft network composite materials with deterministic and bio-inspired designs, *Nature Commun.* 6 (2015) 6566.
- [2] Y. Gao, J. Song, S. Li, C. Elowsky, Y. Zhou, S. Ducharme, Y.M. Chen, Q. Zhou, L. Tan, Hydrogel microphones for stealthy underwater listening, *Nature Commun.* 7 (2016) 12316.
- [3] J. Li, D.J. Mooney, Designing hydrogels for controlled drug delivery, *Nat. Rev. Mater.* 1 (2016) 16071.
- [4] C.C. Kim, H.H. Lee, K.H. Oh, J.Y. Sun, Highly stretchable, transparent ionic touch panel, *Science* 353 (2016) 682–687.
- [5] C. Hoeve, P. Flory, The elastic properties of elastin, *Biopolymers* 13 (1974) 677–686.
- [6] D. Urry, C. Venkatachalam, K. Prasad, R. Bradley, G. Parenti-Castelli, G. Lenaz, Conduction processes of the gramicidin channel, *Int. J. Quantum Chem.* 20 (1981) 385–399.
- [7] Y. Chen, Z. Guan, Bioinspired modular synthesis of elastin-mimic polymers to probe the mechanism of elastin elasticity, *J. Am. Chem. Soc.* 132 (2010) 4577.
- [8] P.D. Wu, E.V.D. Giessen, On improved network models for rubber elasticity and their applications to orientation hardening in glassy polymers, *J. Mech. Phys. Solids* 41 (1993) 427–456.
- [9] J.S. Bergström, M.C. Boyce, Constitutive modeling of the large strain time-dependent behavior of elastomers, *J. Mech. Phys. Solids* 46 (1998) 931–954.
- [10] C. Miehe, S. Göktepe, F. Lulei, A micro-macro approach to rubber-like materials-Part I: the non-affine micro-sphere model of rubber elasticity, *J. Mech. Phys. Solids* 52 (2004) 2617–2660.
- [11] C. Miehe, S. Göktepe, A micro-macro approach to rubber-like materials. Part II: The micro-sphere model of finite rubber viscoelasticity, *J. Mech. Phys. Solids* 53 (2005) 2231–2258.
- [12] M.C. Boyce, E.M. Arruda, Constitutive models of rubber elasticity: A review, *Rubber Chem. Technol.* 73 (2012) 504–523.
- [13] S. Tang, S. Greene, Liu, W. Kam, Two-scale mechanism-based theory of nonlinear viscoelasticity, *J. Mech. Phys. Solids* 60 (2012) 199–226.
- [14] Z. Du, X. Guo, Variational principles and the related bounding theorems for bi-modulus materials, *J. Mech. Phys. Solids* 73 (2014) 183–211.
- [15] M. Latorre, M. Mohammadkhah, C.K. Simms, F.J. Montáns, A continuum model for tension-compression asymmetry in skeletal muscle, *J. Mech. Behav. Biomed. Mater.* 77 (2018) 455–460.
- [16] G.A. Francfort, J.J. Marigo, Revisiting brittle fracture as an energy minimization problem, *J. Mech. Phys. Solids* 46 (1998) 1319–1342.
- [17] D. Mumford, J. Shah, Optimal approximations by piecewise smooth functions and associated variational problems, *Comm. Pure Appl. Math.* 42 (1989) 577–685.
- [18] L. Ambrosio, V.M. Tortorelli, Approximation of functional depending on jumps by elliptic functional via Γ -convergence, *Comm. Pure Appl. Math.* 43 (1990) 999–1036.
- [19] C. Miehe, M. Hofacker, F. Welschinger, A phase field model for rate-independent crack propagation: Robust algorithmic implementation based on operator splits, *Comput. Methods Appl. Mech. Engrg.* 199 (2010) 2765–2778.
- [20] C. Miehe, F. Welschinger, M. Hofacker, Thermodynamically consistent phase-field models of fracture: Variational principles and multi-field FE implementations, *Internat. J. Numer. Methods Engrg.* 83 (2010) 1273–1311.
- [21] C.J. Larsen, C. Ortner, Existence of solutions to a regularized model of dynamic fracture, *Math. Models Methods Appl. Sci.* 20 (2010) 1021–1048.
- [22] C.J. Larsen, *Models for Dynamic Fracture Based on Griffith's Criterion*, Springer Netherlands, 2010, pp. 131–140.
- [23] B. Bourdin, C.J. Larsen, C.L. Richardson, A time-discrete model for dynamic fracture based on crack regularization, *Int. J. Fract.* 168 (2010) 133–143.
- [24] M.J. Borden, C.V. Verhoosel, M.A. Scott, T.J.R. Hughes, C.M. Landis, A phase-field description of dynamic brittle fracture, *Comput. Methods Appl. Mech. Engrg.* 217–220 (2012) 77–95.
- [25] M. Hofacker, C. Miehe, A phase field model of dynamic fracture: Robust field updates for the analysis of complex crack patterns, *Internat. J. Numer. Methods Engrg.* 93 (2013) 276–301.
- [26] C. Kuhn, R. Müller, A continuum phase field model for fracture, *Eng. Fract. Mech.* 77 (2010) 3625–3634.
- [27] F.P. Duda, A. Ciarbonetti, P.J. Sánchez, A.E. Huespe, A phase-field/gradient damage model for brittle fracture in elastic-plastic solids, *Int. J. Plast.* 65 (2014) 269–296.
- [28] M. Ambati, T. Gerasimov, L. De Lorenzis, A review on phase-field models of brittle fracture and a new fast hybrid formulation, *Comput. Mech.* 55 (2015) 383–405.
- [29] C. Miehe, M. Hofacker, L.M. Schänzel, F. Aldakheel, Phase field modeling of fracture in multi-physics problems. Part II. Coupled brittle-to-ductile failure criteria and crack propagation in thermo-elastic-plastic solids, *Comput. Methods Appl. Mech. Engrg.* 294 (2015) 486–522.
- [30] M. Ambati, T. Gerasimov, L. De Lorenzis, Phase-field modeling of ductile fracture, *Comput. Mech.* 55 (2015) 1017–1040.
- [31] C. Mcauliffe, H. Waisman, A unified model for metal failure capturing shear banding and fracture, *Int. J. Plast.* 65 (2015) 131–151.
- [32] M. Ambati, R. Kruse, L. De Lorenzis, A phase-field model for ductile fracture at finite strains and its experimental verification, *Comput. Mech.* 57 (2016) 149–167.
- [33] M.J. Borden, T.J.R. Hughes, C.M. Landis, A. Anvari, I.J. Lee, A phase-field formulation for fracture in ductile materials: Finite deformation balance law derivation, plastic degradation, and stress triaxiality effects, *Comput. Methods Appl. Mech. Engrg.* 312 (2016) 130–166.
- [34] C. Miehe, L.M. Schänzel, Phase field modeling of fracture in rubbery polymers. Part I: Finite elasticity coupled with brittle failure, *J. Mech. Phys. Solids* 65 (2014) 93–113.
- [35] C.H. Chen, E. Bouchbinder, A. Karma, Instability in dynamic fracture and the failure of the classical theory of cracks, *Nat. Phys.* 13 (2017) 1186.
- [36] M. Arriaga, H. Waisman, Combined stability analysis of phase-field dynamic fracture and shear band localization, *Int. J. Plast.* 96 (2017) 81–119.

- [37] H. Amor, J.J. Marigo, C. Maurini, Regularized formulation of the variational brittle fracture with unilateral contact: Numerical experiments, *J. Mech. Phys. Solids* 57 (2009) 1209–1229.
- [38] C. Hesch, K. Weinberg, Thermodynamically consistent algorithms for a finite-deformation phase-field approach to fracture, *Internat. J. Numer. Methods Engrg.* 99 (2015) 906–924.
- [39] B. Bourdin, G.A. Francfort, J. Marigo, Numerical experiments in revisited brittle fracture, *J. Mech. Phys. Solids* 48 (2000) 797–826.
- [40] J.D. Davidson, N.C. Goulbourne, A nonaffine network model for elastomers undergoing finite deformations, *J. Mech. Phys. Solids* 61 (2013) 1784–1797.
- [41] Y. Li, S. Tang, M. Kröger, W.K. Liu, Molecular simulation guided constitutive modeling on finite strain viscoelasticity of elastomers, *J. Mech. Phys. Solids* 88 (2016) 204–226.
- [42] M. Arriaga, C. McAuliffe, H. Waisman, Onset of shear band localization by a local generalized eigenvalue analysis, *Comput. Methods Appl. Mech. Engrg.* 289 (2015) 179–208.
- [43] T.F. Guo, W.H. Wong, Void-sheet analysis on macroscopic strain localization and void coalescence, *J. Mech. Phys. Solids* 118 (2018) 172–203.
- [44] S. Tang, A.M. Kopacz, S. Chan O’Keeffe, G.B. Olson, W.K. Liu, Concurrent multiresolution finite element: Formulation and algorithmic aspects, *Comput. Mech.* 52 (2013) 1265–1279.
- [45] N.A. Hocine, M.N. Abdelaziz, A. Imad, Fracture problems of rubbers: J-integral estimation based upon η factors and an investigation on the strain energy density distribution as a local criterion, *Int. J. Fract.* 117 (2002) 1–23.